

Supporting Information for

Fast photoelectron transfer in $C_{\text{ring}}\text{-C}_3\text{N}_4$ plane-heterostructural nanosheets for overall water splitting

Wei Che[†], Weiren Cheng[†], Tao Yao, Fumin Tang, Wei Liu, Hui Su, Yuanyuan Hang, Qinghua Liu,* Jinkun Liu, Fengchun Hu, Zhiyun Pan, Zhihu Sun, and Shiqiang Wei*

National Synchrotron Radiation Laboratory, University of Science and Technology of China, Hefei 230029, Anhui, P. R. China

S1. Materials

In-plane thermal-conjugate $C_{\text{ring}}\text{-C}_3\text{N}_4$. The synthesis of in-plane heterostructure $C_{\text{ring}}\text{-C}_3\text{N}_4$ undergoes three well-designed steps: melem forming, triazine-carbon ring unit constructing, and final polymerization. For a typical process, 10 g melamine powder was completely dispersed into 50 mL (16 g/L) glucose solution under an ultrasonic bath at 50 °C for 30 min, and then the mixed solution was dried in 60 °C drying baker for overnight to entirely remove water. After that, the mixed resultants sequentially went through three stages of heating: 300 °C for 1h, 400 °C for 1h and 550 °C for 4 h. After naturally cooling down to room temperature, the final product with brown-color was collected and grinded for further characterization.

Thermal-conjugate g- $C_3\text{N}_4$. Typically, graphitic carbon nitride was synthesized by thermal treatment of melamine (10 g, AR, Sinopharm Chemical Reagent Co. Ltd) under 550 °C for 4 hours. After cooling down to room temperature, the yellow-colored product was obtained and was collected and grinded into fine powder for further use. Then, the sample labeled as pristine $C_3\text{N}_4$ was washed by DI water to remove residual species adsorbed on the sample surface and dried at 60 °C overnight.

Thermal-conjugate graphite. For comparison, the graphite carbon (g-C) was prepared by directly heated glucose molecule under 550 °C for 4 h and then was grinded into fine power for further used.

All of C_3N_4 , graphite, and $C_{ring}\text{-}C_3N_4$ are washed by DI water for several times to completely remove residual species after the heating treatment. Besides, a further purification strategy via hydrothermal treatment was also conducted to remove the unstable small fragment from the final product. The typical purification process is as follows: 1) $C_{ring}\text{-}C_3N_4$ nanosheets were washed by DI water for three times after heating treatment to remove residual water-soluble species; 2) the resultant $C_{ring}\text{-}C_3N_4$ nanosheets were dispersed in 0.5 M HNO_3 aqueous solution by ultrasonication for 1 h and then was maintained at 80 °C for 2 h to remove amide impurity; 3) the final products were collected by centrifugation, washed with ethanol, and then washed with deionized water for several times.

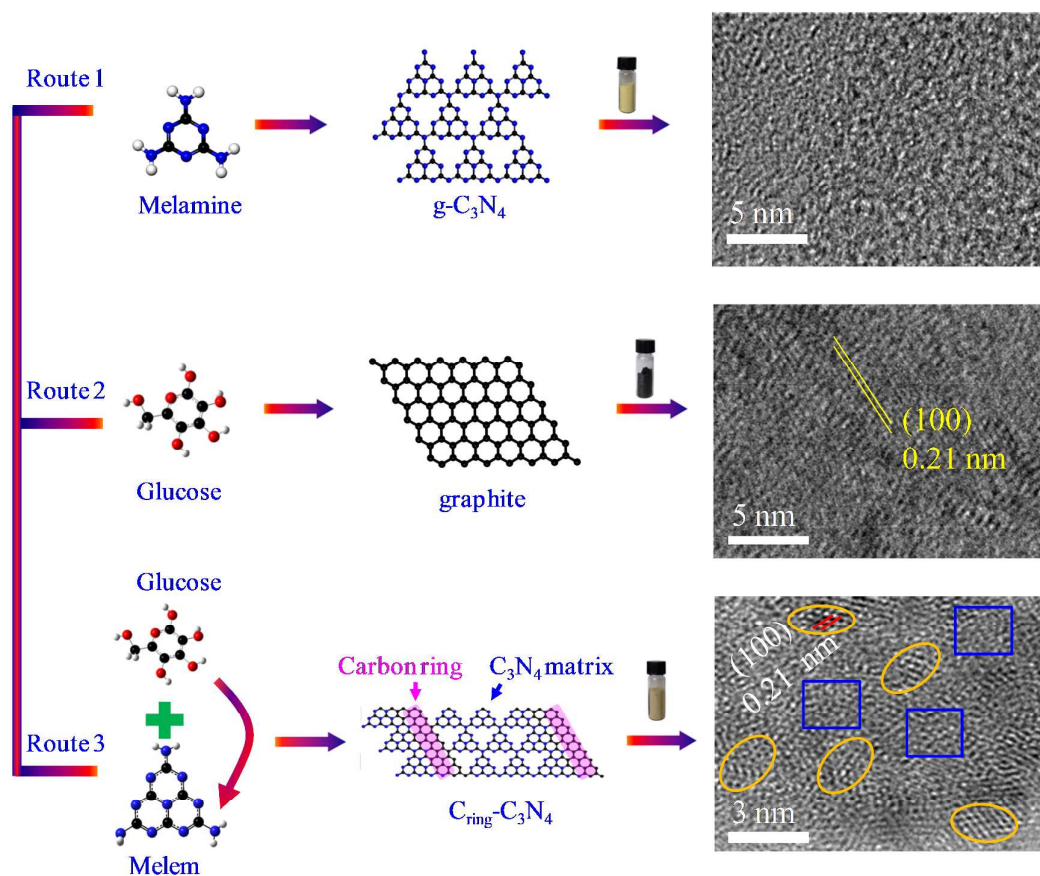
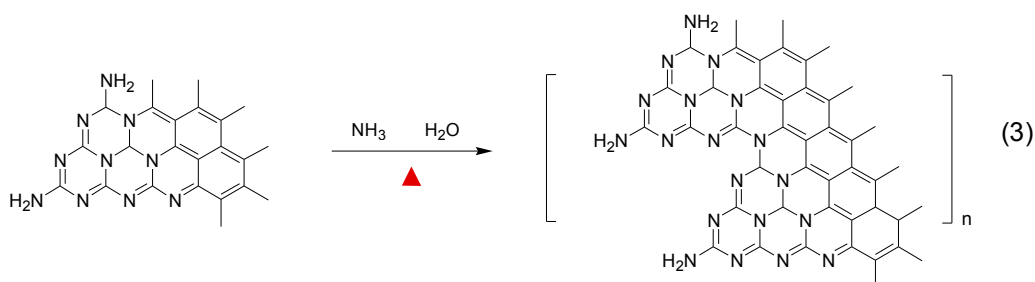
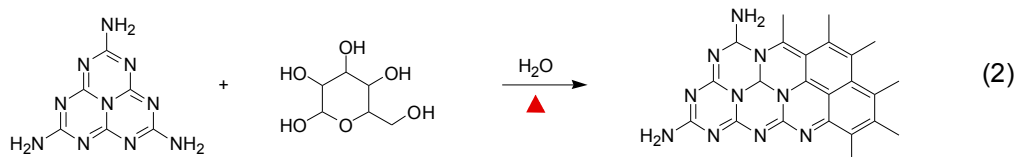
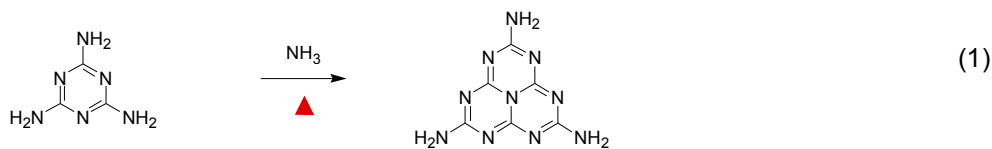


Figure S1. The thermal polymerization procedures for pristine $g\text{-}C_3N_4$, graphite, and heterostructure $C_{ring}\text{-}C_3N_4$.

In the initial stage of the $C_{ring}\text{-}C_3N_4$ synthetic process, the melem was quickly

formed from melamine precursor via deamination reaction at relatively low temperature. Subsequently, the nucleophilic attack of the amino group of melam by hydroxyl groups of glucose was occurred and then the novel sp^2 hybridization of C and N was formed through dehydration reaction, leading to the cyclized in-plane heterostructural unit. Finally, these heterostructural motifs undergo further polymerization to form the final in-plane $C_{ring}-C_3N_4$ heterostructure nanosheets with the elevated temperature. The corresponding chemical transformation processes can be described by the following chemical equations (1), (2), and (3).



S2. Materials characterization

The XRD patterns were performed on Philips X'Pert Pro Super X-ray diffractometer with Cu $K\alpha$ radiation. The SEM measurements were conducted using a scanning electron microscope (JSM-6700F, and 5kV). The UV-vis spectra (DRS) were recorded on a Shimadzu DUV-3700 spectrophotometer. Transmission electron microscopy (TEM), High-resolution transmission electron microscopy (HRTEM) and energy dispersive X-ray spectra (EDS) analysis were performed on a JEM-2100F microscope at an acceleration voltage of 200 kV. The TG-DSC curves were recorded on SDT Q600 V20.9 thermal analysis instruments at a heating rate of 5 °C/min under

the air. Photoluminescence (PL) measurements were recorded with an excitation wavelength of 360 nm. X-ray photoelectron spectra (XPS) were acquired on an ESCALAB MKII with Mg K α ($h\nu = 1253.6$ eV) as the excitation source. The binding energies obtained in the XPS spectral analysis were corrected for specimen charging by referencing C 1s to 284.5 eV.

As Figure S2 shown, the colors of melamine and glucose are white, but the melamine seems more exquisite than that of glucose. After heating treatment, the colors of melamine, glucose, and melamine-glucose mixture turn yellow, black, and brown, respectively, indicating the formation of various products corresponding to g-C₃N₄, graphite, and C_{ring}-C₃N₄. In contrast to the graininess graphite (Figure S3), both of g-C₃N₄ and C_{ring}-C₃N₄ display sheet-like morphology, which inevitably stacked to each other due to the high concentration during preparation of SEM measurement. The edges of the flexible C_{ring}-C₃N₄ nanosheets spontaneously curl upon drying due to the ultrathin nature and there is no any secondary morphology on their smooth surface (Figure S3c), evidently demonstrating the absence of obvious carbon dot after heating treatment.

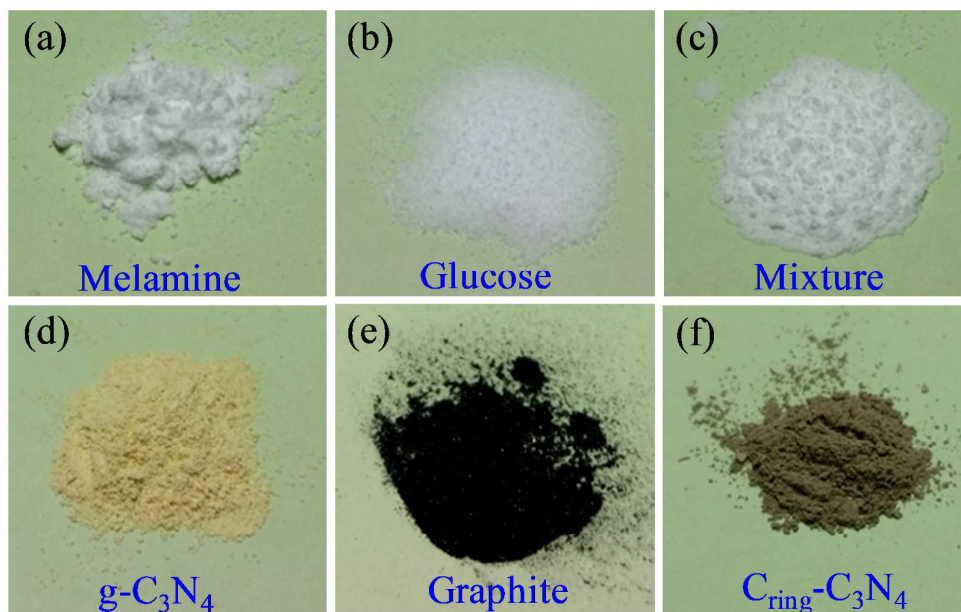


Figure S2. Photographs of the polymeric precursors and corresponding final products. (a–c) melamine, glucose, and melamine-glucose mixture. (d–f) g-C₃N₄, graphite, and C_{ring}-C₃N₄.

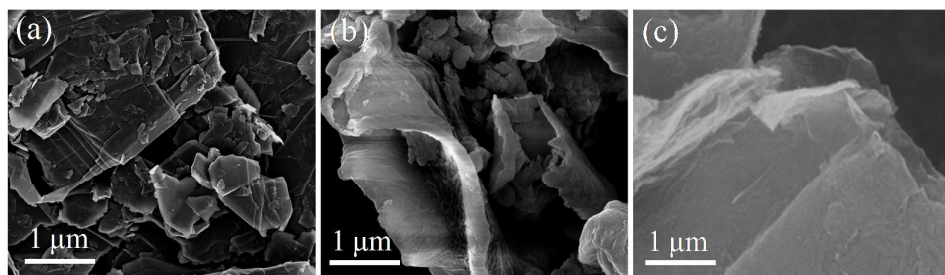


Figure S3. SEM images for the samples. (a) graphite, (b) pristine C_3N_4 , and (c) $C_{ring}-C_3N_4$.

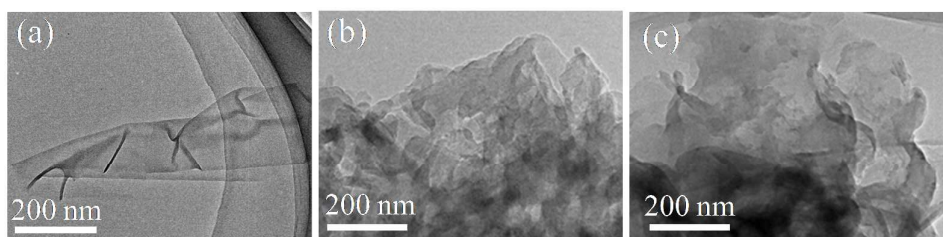


Figure S4. Typical TEM images for (a) graphite, (b) pristine C_3N_4 , (c) $C_{ring}-C_3N_4$.

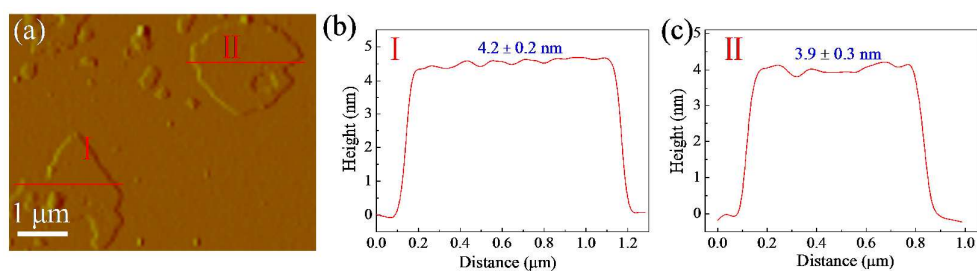


Figure S5. AFM image and corresponding profiles for $C_{ring}-C_3N_4$.

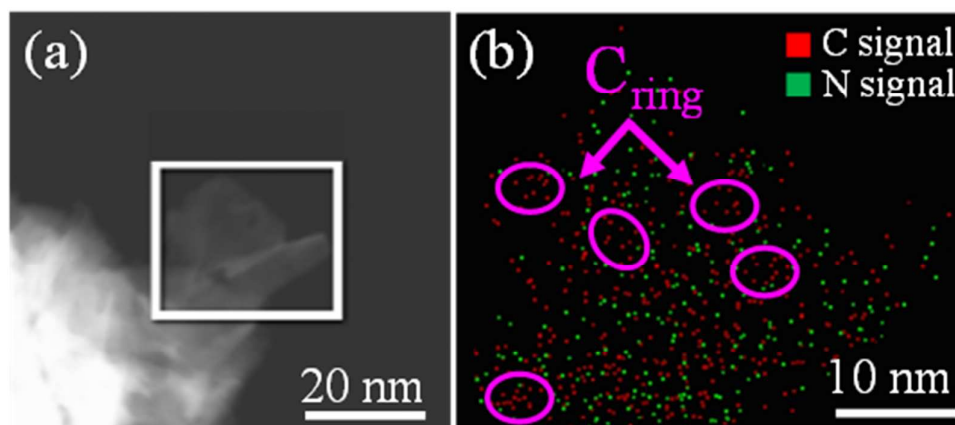


Figure S6. TEM-EDS mapping images. (a) TEM image, and (b) C and N mapping image.

As Figure S3c shown, the SEM image displays flexible ultrathin nanosheet of

$C_{\text{ring}}\text{-}C_3N_4$ with smooth surface without any second morphology growth atop from a broader vision. Furthermore, AFM image in Figure S5 presents that the surface fluctuation of $C_{\text{ring}}\text{-}C_3N_4$ nanosheet is only $\pm 0.2\text{--}0.3$ nm, far less than the size of carbon dot (5–10 nm), indicating the absence of carbon dot or other C-contained impurity on the surface of $C_{\text{ring}}\text{-}C_3N_4$ nanosheet.

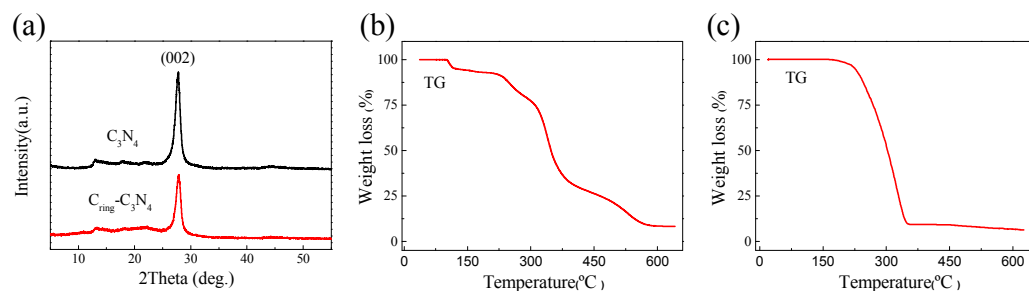


Figure S7. (a) XRD pattern; Thermogravimetric analysis results of glucose (b) and melamine (c).

Ultraviolet photoemission spectroscopy (UPS) characterization. Photoemission spectroscopy experiments were performed at the Catalysis and Surface Science Endstation at the BL11U beamline in the National Synchrotron Radiation Laboratory (NSRL). The beamline is connected to an undulator and equipped with two gratings that offer soft X-rays from 20 to 600 eV with a typical photon flux of 5×10^{10} photons/s and a resolution ($E/\Delta E$) better than 10^4 at 29 eV. The density of states for valence-band photoelectron spectra by the ultraviolet photoemission spectroscopy (UPS) characterization is applied to explore the chemical state and the information for bonding structure of the solid surface. The Fermi level E_F is located at $E=0$ which was measured from the Fermi edge of an evaporated Au film. The work function measurements were also conducted with that to allow the observation of the secondary electron cut-off. The sample was biased by -5.0 V in order to acquire distinct the secondary-electron cutoff of the spectrum and Valence band spectrum chosen for 20 eV of synchrotron radiation light excitation energy. During the process of experiment, the standard samples of Au 4f spectral peak and Fermi edge was used for photon energy calibration. The energy differences between the vacuum level (VL) and the Fermi level corresponds to the work function (WF) of the samples which reflect the changes of the fine structure on the surface.

XANES measurements. The C and N *K*-edge X-ray absorption near-edge spectra (XANES) were measured at BL12B-a beamline of National Synchrotron Radiation Laboratory (NSRL, China) in the total electron yield (TEY) mode by collecting the sample drain current under a vacuum better than 5×10^{-8} Pa.^{1,2} The beam from the bending magnet was monochromatized utilizing a varied linespacing plane grating and refocused by a toroidal mirror. The energy range is 100–1000 eV with an energy resolution of ca. 0.2 eV. For the XANES measurement, incident X-ray beam with the “magic angle” of 54.7° and high energy resolution of 0.1 eV were used. During the XANES measurement, the samples were firmly adhered on the conductive substrate with random orientation, so the polarization dependence is not considered here.

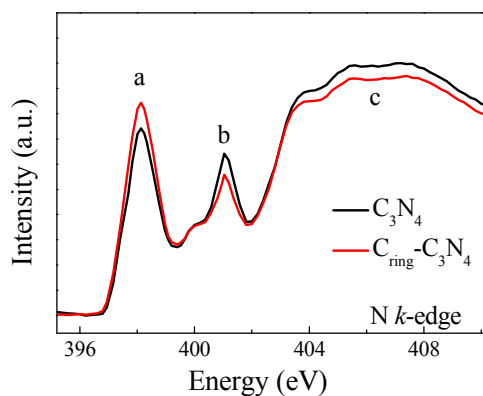


Figure S8. N *K*-edge X-ray absorption near edge structure (XANES) spectroscopy.

The XPS spectrum was deconvoluted to offer more information about the compositions and chemical environment of pure g- C_3N_4 and C_{ring} - C_3N_4 as depicted in Figure S5. For C 1s of pure g- C_3N_4 , peaks at 288.2 eV, 287.5 eV and 284.6 eV was assigned to sp^2 -hybridized C-N in triazine, C bonded with amino group and defect C-C respectively.^{3,4,5} Apparently, the contribution of 284.6 eV peak for C_{ring} - C_3N_4 is significant larger than that of pure C_3N_4 (13.88% verse 0.42%), indicating the incorporation of carbon-ring. Moreover, The changed contribution ratio of ~ 399 eV to ~ 398 eV peaks also confirmed the π -conjugate bond between edge N in triazine with C of Carbon-ring, where the peaks at ~ 398 , 399, 400 and 401 eV can be indexed to sp^2 hybridized C-N=C, tertiary N (N-(C)3) groups and amino functional

groups (C-N-H), respectively. According to the XPS and EDS results, the ratio of triazine to carbon-ring was estimated to be around 6:1.

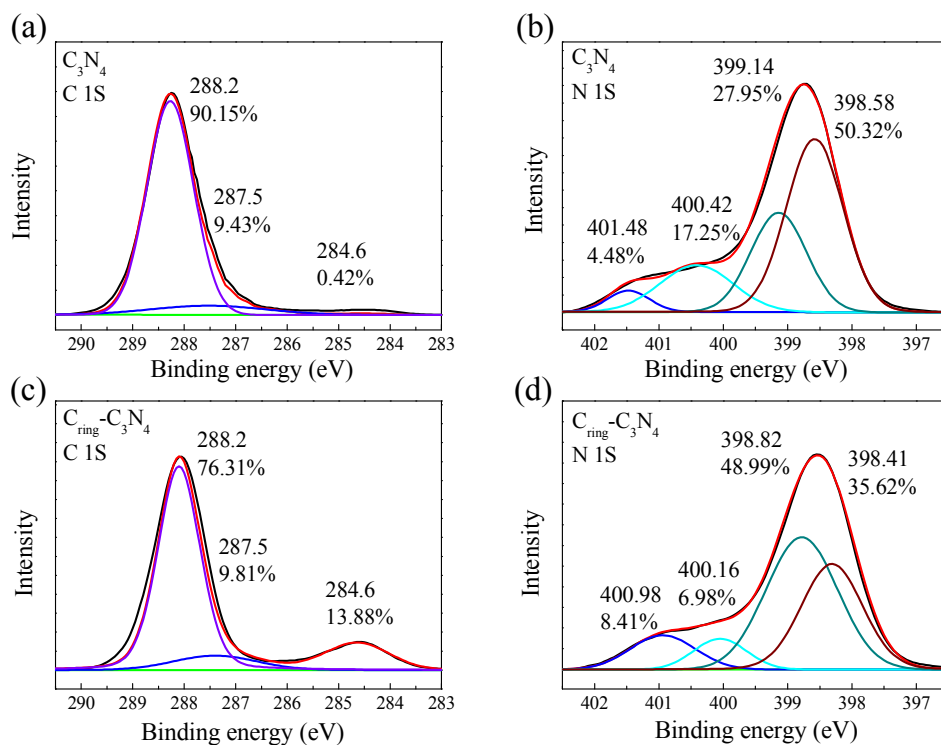


Figure S9. C 1s, N 1s high-resolution XPS spectra for pristine C_3N_4 and $C_{ring}-C_3N_4$.

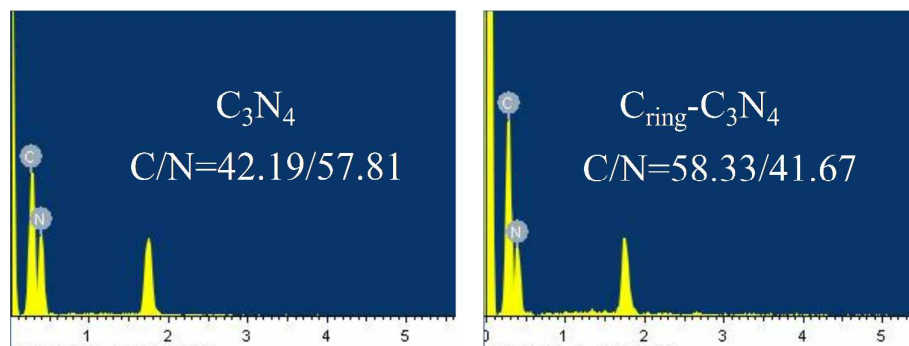


Figure S10. EDS spectra of pristine C_3N_4 and $C_{ring}-C_3N_4$. The additional peak of Si at ~ 1.7 keV was attributed to Si substrate.

Electrochemical measurement methods. Electrochemical measurements were performed using an electrochemical workstation (Model CHI760D, CH instruments, Inc., Austin, TX) with a standard three-electrode photoelectrochemical cell and was

used to record transient photocurrent behavior of the samples, where the prepared electrodes immersed in a sodium sulfate electrolyte solution (0.5 M), a gauze platinum and Ag/AgCl (saturated KCl) act as the working, auxiliary, and reference electrode, respectively. The working electrodes were prepared as follows: First, fluoride tin oxide (FTO) glass was washed sequentially with acetone, ethanol and DI water in an ultrasonic bath for 30 min. Next, 0.05 g of photocatalyst was ground with 5 μ L nafion (5 wt%, Sigma Aldrich) and mixed with 2 mL of acetone under sonication for 30 min to obtain slurry. Then, the slurry was coated onto 1 cm \times 2 cm FTO glass electrode by the spin coater. After air-drying, the electrodes were sintered at 350 $^{\circ}$ C for 120 min to improve adhesion. In addition, the three electrodes were immersed in a sodium sulfate electrolyte solution (0.5 M) as conductive media at pH 6.8, which was continuously in an N₂-purged flow to remove O₂ before light irradiation. Photocurrent measurements utilized a 300 W Xe lamp. The working electrode was back-illuminated through the FTO glass in order to minimize absorption by the dark and thick catalyst layer. Capacitance was measured to obtain Mott-Schottky plots for working electrodes at potential window ranged from -1.0 to -0.2 V, and the perturbation signal was an AC voltage magnitude of 50 mV with the frequency at 3 kHz. The electrochemical impedance spectroscopy (EIS) was measured at -1.4 V (vs. RHE), and the perturbation signal was also 5 mV with the frequency ranged from 0.1 Hz to 100 kHz.

Photocatalytic reactions and measurements. Photocatalytic overall water splitting reactions were carried out in a top-irradiation-type photoreactor (Pyrex glass) connected to a closed gas circulation system. Approximately 30 mg of the photocatalysts were dispersed in 100 ml DI-water without sacrificial electron donor and the deposition of ~3 wt % Pt cocatalyst was conducted by directly dissolving trace H₂PtCl₆·6H₂O into the above 100 mL reaction solution. The reactant solution was evacuated several times to remove air thoroughly and irradiated using a 300 W Xe-lamp (PLS-SXE 300, Beijing perfectlight Co. Ltd, China). The generated hydrogen and oxygen were measured by a gas chromatograph (GC) equipped with a

thermal conduction detector (TCD, 5 Å molecular sieve columns with 3 m length) using Ar as carrier gas with flow rate of 20 ml/min. The injection port, column, and detector temperatures are 60, 60, and 130 °C, respectively. The 60 cycles with time interval of 6 hours were performed. The quantum efficiency (QE) was calculated from equation as follows,⁶

$$QE = \frac{2 \times \text{the number of evolved } H_2 \text{ molecules}}{\text{the number of incident photons}} \times 100\% \quad (1)$$

Several band-pass filters (FWHM=15 nm) were employed to achieve a different incident light wavelength under a 300 W Xe lamp for measurement of the quantum efficiency. The average intensity of each irradiation wavelength was determined by an optical power meter (PM100D, Thermal Powermeter Head, THORLABS).

For full spectrum measurement, a 300 W xenon arc lamp (PLS-SXE300/300UV) with a standard AM1.5 filter, outputting the light density of 100 mW/cm², was used as illumination source to trigger the photocatalytic reaction for pristine C₃N₄ and C_{ring}-C₃N₄ nanosheets. Subsequently, a 420 nm cutoff filter was added to remove the light whose wavelength is shorter than 420 nm, and then the visible-light region of ≥ 420 nm was obtained as illumination source to activate photocatalytic reaction. As for the photocatalytic performance under UV light (<420nm), it is calculated by subtracting visible-light (≥ 420 nm) hydrogen evolution yield from full production capacity illuminated under the overall spectrum.

The photoresponse of the prepared photoelectrodes (I-t) was operated by measuring the photocurrent densities under chopped light irradiation (light on/off cycles: 20s) at a bias potential of -0.4 V vs. Ag/AgCl. The transient open-circuit voltage decay (OCVD) measurements were taken for 800 s in all, and the light on and off were controlled at 200 s and 400 s from the start, respectively. The average lifetime of the photogenerated carriers (τ_n) were obtained from the OCVD according to Equation (2):⁷

$$\tau_n = -\frac{k_B T}{q} \left(\frac{dV_{OC}}{dt} \right)^{-1} \quad (2)$$

Where k_B is the Boltzmann constant, T is the temperature (in Kelvin), and q is the unsigned charge of an electron.

The impedance of charge diffusion and recombination mechanism derived from Equation (3):⁸

$$Z = \left(\frac{R_w R_k}{1 + i\omega / \omega_k} \right)^{1/2} \tanh[(\omega_k / \omega_d)^{1/2} (1 + i\omega / \omega_k)^{1/2}] \quad (3)$$

Where $L_{charge} / L = (\omega_d / \omega_k)^{1/2}$, ω_d and ω_k are the characteristic frequency of charge diffusion and reaction respectively, R_w and R_k are the characteristic resistance of charge diffusion and reaction respectively.

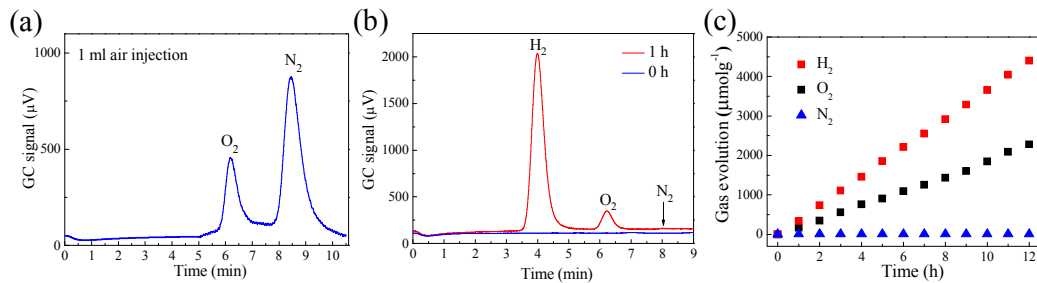


Figure S11. (a) GC signal for 1 ml air; (b) GC signal for photocatalytic activity of in-plane heterostructure $C_{ring}-C_3N_4$ nanosheets after 1 h light illumination; (c) gas evolution of in-plane heterostructure $C_{ring}-C_3N_4$ nanosheets during photocatalytic test.

1 ml air was injected into the gas-closed circulation system with Ar as carrier gas to confirm both N_2 and O_2 can be detected by gas chromatography ($\sim 5 \mu\text{l}$ air into GC system through sample loop). It can be seen that significant O_2 and N_2 peaks located at 6.2 and 8.5 min was observed in Figure S11a, respectively. Subsequently, the photocatalytic was thoroughly degassed to remove the air for the following photocatalytic test of $C_{ring}-C_3N_4$ nanosheets. In comparison, only H_2 and O_2 peaks at 4 and 6.2 min was detected during the photocatalytic measurement of $C_{ring}-C_3N_4$

nanosheets after 1 hour light illumination as shown in Figure S11b, and hardly any N_2 was detected even after 12 h operation (Figure S11c). The absence of N_2 and the stoichiometric ratio of $\sim 2:1$ for H_2 and O_2 gases evidently confirmed that the observed O_2 gas exactly comes from photocatalytic water splitting by $C_{ring}-C_3N_4$ nanosheets rather than leakage air. Moreover, the unchanged N_2 gas with increase irradiation time demonstrated the absence of photocorrosion during photocatalytic reaction, indicating super photocatalytic stability for $C_{ring}-C_3N_4$ nanosheets.

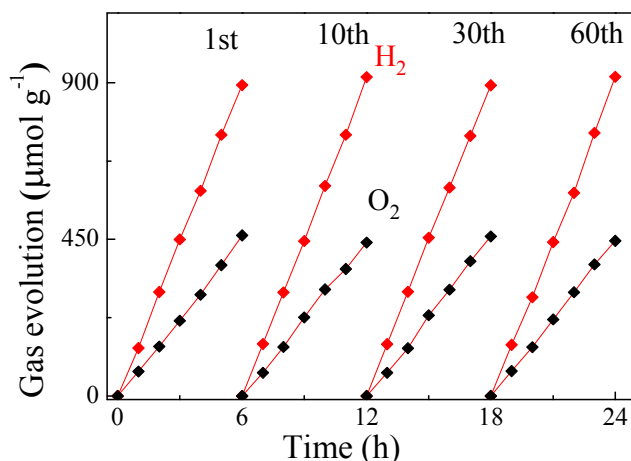


Figure S12. Typical time course of hydrogen and oxygen production in pure water under irradiation of ≥ 420 nm.

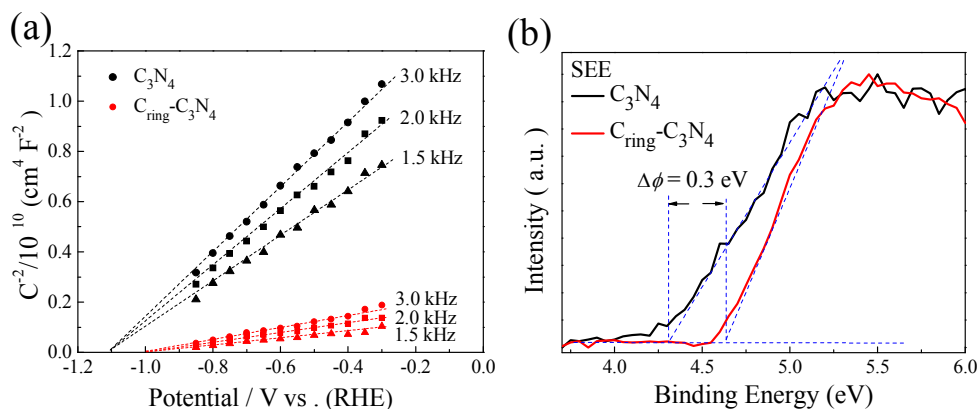


Figure S13. (a) Mott-Schottky plots and (b) Second electron emission spectra (SEE).

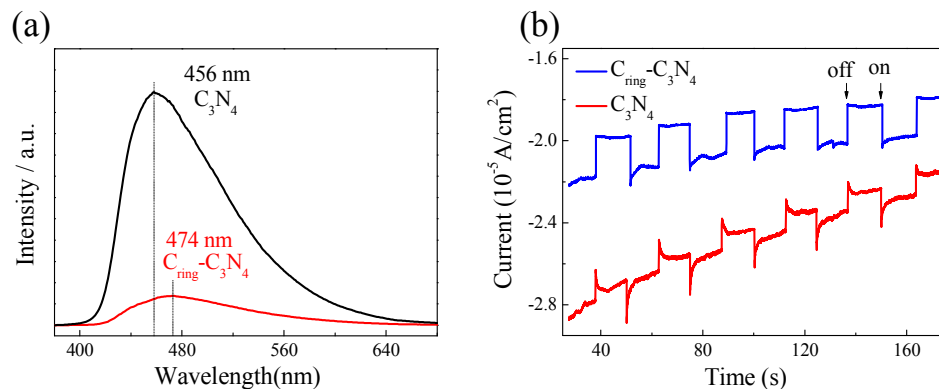


Figure S14. Photoluminescence emission curves and photocurrent transient measurements.

Table S1. Summary of the overall water splitting performance of g-C₃N₄ based catalysts.

Catalysts	pure water system	catalysts mass	cocatalysts	Light source	Incident light/nm	H ₂ Rate (μmol/h/g)	O ₂ Rate (μmol/h/g)	(Ref.)
polypyrrole (PPy)/g-C ₃ N ₄	pure water	100mg	3 wt% Pt	300 W Xe lamp	>400 nm	154	—	9
g-C ₃ N ₄ / BiVO ₄	pure water	300mg	3 wt% Pt	300 W Xe lamp	>395 nm	36	18	10
g-C ₃ N ₄ / WO ₃	pure water	—	1 wt% Pt	300 W Xe lamp	>395 nm	74	37	10
TiO ₂ /C ₃ N ₄ -Ni(OH) ₂ /WO ₃ (PtOx)	pure water (NaI)	200mg	1 wt% Pt	150 W Xe lamp	>200 nm	251	121	11
TiO ₂ /g-C ₃ N ₄ -WO ₃ (1%PtOx)	pure water (FeCl ₂)	200mg	1 wt% Pt	150 W Xe lamp	>200 nm	29.4	14.3	11
TiO ₂ /g-C ₃ N ₄ -Ni(OH) ₂ /WO ₃	pure water (NaI)	200mg	1 wt% Pt	150 W Xe lamp	>200 nm	49	26	11
g-C ₃ N ₄	pure water	200mg	3 wt% Pt 1 wt% Co	300 W Xe lamp	>300 nm	61	31	12
Co ₃ O ₄ /HCNS/Pt	pure water	20mg	1 wt% Pt	300 W Xe lamp	>300 nm	155	75	13
CoP/g-C ₃ N ₄	pure water	80mg	3 wt% Pt	300 W Xe lamp	>300 nm	250	125	14
C-dot/C ₃ N ₄	Pure water	80mg	—	300 W Xe lamp	>420 nm	575	—	15
g-C ₃ N ₄	pure water	30mg	3 wt% Pt	300 W Xe lamp	>300 nm	53	25	this work
C _{ring} -g-C ₃ N ₄	pure water	30mg	3 wt% Pt	300 W Xe lamp	>300 nm	371	184	this work

S3. DFT calculation details

The first-principles density functional theory (DFT) calculations were performed using a plane wave basis set with the projector augmented plane-wave (PAW) method.^{16,17} The exchange-correlation interaction was described within the

generalized gradient approximation (GGA) in the form of PW91.¹⁸ The energy cutoff was set to 400 eV, and the atomic positions were allowed to relax until the energy and force were less than 10^{-4} eV and 10^{-2} eV/Å, respectively. The graphitic carbon nitride was modeled in supercell geometry containing up to four tri-s-triazine units and the graphitic planes were separated by a vacuum region of 15 Å. The C_{ring}-C₃N₄ model consists of four tri-s-triazine and two carbon ring units with the ratio of 6:1 for triazine to carbon ring.

Table S2. Calculated adsorption energy profiles for pristine g-C₃N₄ and C_{ring}-C₃N₄.

Adsorbed species	M'-H ₂ O	M	M-H*	M+H ₂
Pristine g-C ₃ N ₄	1.10 eV	0.00 eV	1.12 eV	-0.11 eV
C _{ring} -C ₃ N ₄	0.9 eV	0.00 eV	0.67 eV	-0.39 eV

Note: M' and M refer to N and C sites, respectively.

References

- [1] Bhattacharyya, S.; Lübke, M.; Richter, F. *J. Appl. Phys.* **2000**, *88*, 5043.
- [2] Roy, S. S.; McCann, R.; Papakonstantinou, P.; McLaughlin, J. A.; Kirkman, I. W.; Bhattacharyya, S.; Silva, S. R. P. *J. Appl. Phys.* **2006**, *99*, 043511.
- [3] Ma, T. Y.; Dai, S.; Jaroniec, M.; Qiao, S. Z. *Angew. Chem. Int. Ed.* **2014**, *53*, 7281.
- [4] Zhang, S.; Li, J.; Zeng, M.; Li, J.; Xu, J.; Wang, X. *Chem. -Eur. J.* **2014**, *20*, 9805.
- [5] Zheng, Y.; Jiao, Y.; Zhu, Y.; Li, L. H.; Han, Y.; Chen, Y.; Du, A.; Jaroniec, M.; Qiao, S. Z. *Nature Commun.* **2014**, *5*, 3783.
- [6] Huang, J.; Shang, Q.; Huang, Y.; Tang, F.; Zhang, Q.; Liu, Q.; Jiang, S.; Hu, F.; Liu, W.; Luo, Y.; Yao, T.; Jiang, Y.; Pan, Z.; Sun, Z.; Wei, S. *Angew. Chem. Int. Ed.* **2016**, *55*, 2137.

- [7] Bai, S.; Yang, L.; Wang, C.; Lin, Y.; Lu, J.; Jiang, J.; Xiong, Y. *Angew. Chem. Int. Ed.* **2015**, *54*, 14810.
- [8] Bisquert, J. *J. Phys. Chem. B* **2002**, *106*, 325.
- [9] Sui, Y.; Liu, J.; Zhang, Y.; Tian, X.; Chen, W. *Nanoscale* **2013**, *5*, 9150.
- [10] Martin, D. J.; Reardon, P. J.; Moniz, S. J.; Tang, J. *J. Am. Chem. Soc.* **2014**, *136*, 12568.
- [11] Yan, J.; Wu, H.; Chen, H.; Zhang, Y.; Zhang, F.; Liu, S. F. *Appl. Catal. B-Environ.* **2016**, *191*, 130.
- [12] Zhang, G.; Lan, Z. A.; Lin, L.; Lin, S.; Wang, X. *Chem. Sci.* **2016**, *7*, 3062.
- [13] Zheng, D.; Cao, X. N.; Wang, X. *Angew. Chem. Int. Ed.* **2016**, *55*, 11512.
- [14] Pan, Z.; Zheng, Y.; Guo, F.; Niu, P.; Wang, X. *ChemSusChem* **2016**, DOI: 10.1002/cssc.201600850.
- [15] Liu, J.; Liu, Y.; Liu, N. Y.; Han, Y. Z.; Zhang, X.; Huang, H.; Lifshitz, Y.; Lee, S. T.; Zhong, J.; Kang, Z. H. *Science* **2015**, *347*, 970-974.
- [16] Furthmüller, G. K. J. *Computational Materials Science* **1996**, *6*, 15.
- [17] Lebègue, S.; Eriksson, O. *Phys. Rev. B* **2009**, *79*, 1.
- [18] Blöchl, P. E. *Phys. Rev. B* **1994**, *50*, 17953.